molecules

MDPI

Article

Theoretical Study of the Magnetic Mechanism of a Pca21 C_4N_3 Monolayer and the Regulation of Its Magnetism by Gas Adsorption

Dongqiu Zhao [1], Xiao Tang [2,*], Xueying Gao [1], Wanyan Xing [1], Shuli Liu [1], Huabing Yin [3] and Lin Ju [1,*]

[1] School of Physics and Electric Engineering, Anyang Normal University, Anyang 455000, China; dqzhao@aynu.edu.cn (D.Z.); 221101050@stu.aynu.edu.cn (X.G.); 221101039@stu.aynu.edu.cn (W.X.); 01958@aynu.edu.cn (S.L.)
[2] College of Science, Nanjing Forestry University, Nanjing 210037, China
[3] Joint Center for Theoretical Physics, Institute for Computational Materials Science, School of Physics and Electronics, Henan University, Kaifeng 475004, China; yhb@henu.edu.cn
* Correspondence: xiaotang@njfu.edu.cn (X.T.); julin@aynu.edu.cn (L.J.)

Abstract: For metal-free low-dimensional ferromagnetic materials, a hopeful candidate for next-generation spintronic devices, investigating their magnetic mechanisms and exploring effective ways to regulate their magnetic properties are crucial for advancing their applications. Our work systematically investigated the origin of magnetism of a graphitic carbon nitride (Pca21 C_4N_3) monolayer based on the analysis on the partial electronic density of states. The magnetic moment of the Pca21 C_4N_3 originates from the spin-split of the $2p_z$ orbit from special carbon (C) atoms and $2p$ orbit from N atoms around the Fermi energy, which was caused by the lone pair electrons in nitrogen (N) atoms. Notably, the magnetic moment of the Pca21 C_4N_3 monolayer could be effectively adjusted by adsorbing nitric oxide (NO) or oxygen (O_2) gas molecules. The single magnetic electron from the adsorbed NO pairs with the unpaired electron in the N atom from the substrate, forming a N_{sub}-N_{ad} bond, which reduces the system's magnetic moment from 4.00 μ_B to 2.99 μ_B. Moreover, the NO adsorption decreases the both spin-down and spin-up bandgaps, causing an increase in photoelectrical response efficiency. As for the case of O_2 physisorption, it greatly enhances the magnetic moment of the Pca21 C_4N_3 monolayer from 4.00 μ_B to 6.00 μ_B through ferromagnetic coupling. This method of gas adsorption for tuning magnetic moments is reversible, simple, and cost-effective. Our findings reveal the magnetic mechanism of Pca21 C_4N_3 and its tunable magnetic performance realized by chemisorbing or physisorbing magnetic gas molecules, providing crucial theoretical foundations for the development and utilization of low-dimensional magnetic materials.

Keywords: magnetic mechanism; first-principles calculations; gas adsorption; two-dimensional materials

check for updates

Citation: Zhao, D.; Tang, X.; Gao, X.; Xing, W.; Liu, S.; Yin, H.; Ju, L. Theoretical Study of the Magnetic Mechanism of a Pca21 C_4N_3 Monolayer and the Regulation of Its Magnetism by Gas Adsorption. *Molecules* **2024**, *29*, 5194. https://doi.org/10.3390/molecules29215194

Academic Editor: Tilo Söhnel

Received: 9 October 2024
Revised: 29 October 2024
Accepted: 31 October 2024
Published: 2 November 2024

Copyright: © 2024 by the authors. Licensee MDPI, Basel, Switzerland. This article is an open access article distributed under the terms and conditions of the Creative Commons Attribution (CC BY) license (https://creativecommons.org/licenses/by/4.0/).

1. Introduction

Two-dimensional (2D) ferromagnetic materials, capable of atomic-level charge and spin control, are regarded as excellent potential candidates for future memory and logic applications [1]. The 2017 discovery of atomically thin vdW magnets, chromium(III) iodide (CrI_3) [2] and chromium germanium telluride ($CrGeTe_3$) [3], unveiled new opportunities for investigating unique magnetic phenomena in reduced dimensions. Since then, numerous 2D magnets have been discovered, including ferromagnets [4–8], antiferromagnets [9,10], and magnetic topological insulators [11]. These 2D magnets, exhibiting remarkable optical, magnetic, magneto-electric, and magneto-optic properties, are highly valuable for investigating new quantum phenomena in low-dimensional magnetism and for advancing the next generation of spintronic devices. These discoveries have inspired numerous theoretical investigations aimed at elucidating the fundamental mechanisms, predicting novel materials, and designing spintronic devices leveraging 2D magnets [12–14].

In addition to traditional 2D ferromagnetic materials based on transition metals or rare earth elements [15,16], substantial efforts have been focused on the exploration of metal-free 2D ferromagnetic materials, which are more cost-effective and environmentally friendly. However, due to the absence of localized spins, most of the metal-free materials are inherently diamagnetic. Therefore, advanced modifications of the electronic structure of non-metallic materials are needed so that they contain unpaired electrons and magnetic coupling capable of exhibiting ferromagnetism. Two-dimensional graphene has garnered significant attention as a novel electronic material due to its unique electrical properties [17]. It is expected that graphene and similar carbon-based 2D materials could be advantageous in spintronic applications. However, theoretical and experimental studies have demonstrated that most carbon-based 2D materials are inherently nonmagnetic [18]. To address this limitation, various strategies including doping [19,20], hydrogenation [21], and defect engineering [22,23] have been proposed to induce ferromagnetism. However, the application of graphene is also limited by its zero bandgap [24]. Graphite carbon nitride (g-C_3N_4), possessing a large bandgap and structurally similar to graphene, has been thoroughly studied as a typical 2D metal-free material due to its distinct optical and electronic properties, along with its strong chemical and thermal stability [25]. Numerous efforts have primarily concentrated on introducing magnetism into nonmagnetic 2D C_3N_4 through methods such as doping [26–29] and defect engineering [30]. However, achieving long-range magnetic order in the plane using these methods is limited and remains a significant challenge, because the magnetism induced by such doping and modifications is typically localized and lacks long-range magnetic order. Exploring intrinsic metal-free ferromagnetic materials holds promise for overcoming these shortcomings. In a recent breakthrough, a novel form of stable graphitic carbon nitride material (Pca21 C_4N_3 monolayer) has been forecasted through a randomized approach grounded in group and graph theory (RG2) [31]. Our previous theoretical study [32] revealed that the Pca21 C_4N_3 monolayer not only exhibited intrinsic long-range ordered ferromagnetism, but also had a high Curie temperature of 246 K. Additionally, the results of ab initio molecular dynamics (AIMD) simulations demonstrate that the Pca21 C_4N_3 monolayer exhibits excellent thermal stability.

Precious studies have revealed that molecular adsorption presents an efficient method for adjusting the electronic structures and magnetic properties of several 2D materials such as graphene [33], phosphorene [34], MXenes [35], and transition metal dichalcogenides [36]. As a newly discovered two-dimensional non-metallic ferromagnet, Pca21 C_4N_3 holds promise of expanded applications by tuning its electronic structure and magnetic properties through molecular adsorption. To the best of our knowledge, research on regulating the electronic structure and magnetic properties of the Pca21 C_4N_3 monolayer through the adsorption of polar molecules and non-polar molecules has not been reported yet. Herein, first-principles calculations have been employed to comprehensively examine the electronic structure and magnetic properties of both the Pca21 C_4N_3 monolayer and its gas-molecule-adsorbed counterparts.

2. Results and Discussion

2.1. Electronic and Magnetic Properties of Pristine Pca21 C_4N_3 Monolayer

As is known to all, a material's microscopic structure determines its physical and chemical properties. Therefore, to explore the origins of its magnetic and electronic structures, the morphology structure of the Pca21 C_4N_3 monolayer is first investigated in detail. The optimized lattice parameters of Pca21 C_4N_3 are a = 4.16 Å and b = 4.77 Å. The ground-state Pca21 C_4N_3 monolayer exhibits a highly corrugated structure with a thickness of 1.28 Å, where nitrogen (N) atoms occupy both the top-most and bottom-most positions. This pronounced corrugation is likely caused by the lone pair interactions of nitrogen atoms. The Pca21 C_4N_3 monolayer features alternating 12-membered macrocycles and 6-membered microcycles. Both types of cycles are constructed from two kinds of covalent bonds, namely carbon-carbon (C-C) bonds and carbon-nitrogen (C-N) bonds. The lengths of the C-C bonds vary from 1.45 Å to 1.46 Å, averaging at 1.46 Å. Meanwhile, C-N bond lengths

range between 1.34 Å and 1.36 Å, with an average of 1.35 Å. As displayed in Figure S1, each carbon (C) atom bonds with three other atoms. Carbon atoms bonded solely with three other carbon atoms are labeled as C_C, whereas those bonded with one carbon and two nitrogen atoms are designated as C_N. These two types of C exhibit different physical and chemical properties due to differences in their surrounding chemical environments. Additionally, each nitrogen atom is bonded to two C_N atoms. Furthermore, the Pca21 space group belongs to the orthorhombic system and exhibits chiral symmetry. It is characterized by only translational and rotational symmetry operations, with no inversion or mirror symmetry operations of any kind.

The Pca21 C_4N_3 monolayer is fundamentally a modified graphitic C_3N_4, where certain nitrogen atoms are substituted by carbon atoms. Given that one carbon atom has one fewer electrons than one nitrogen atom, the C_4N_3 system features unpaired electrons, which primarily contribute to the magnetism. The electronic structure properties near the Fermi level (E_f) determine the fundamental physical and chemical properties of materials, such as photoelectric activity, catalytic activity, and magnetic performance. To investigate the origin of magnetic performance and the distribution of magnetic moments in the Pca21 C_4N_3 monolayer, we examined the electronic orbitals near the Fermi level of C_C, C_N, and N, as well as the spatial spin density distribution in the pristine monolayer. Figure 1a displays the spin-resolved partial density of states (PDOS) for Pca21 C_4N_3, indicating that the bandgap (E_g) in the spin-down channel is 0.36 eV, whereas the one in the spin-up channel is much larger, reaching 2.24 eV. Near the Fermi level, the valence band (VB) for both the spin-up and spin-down channels is predominantly occupied by N 2*p* electrons, with a minor contribution from C_C 2*p* electrons, and the spin-up channel contains more electrons than the spin-down channel. The conduction band minimum (CBM) in the spin-down channel is mainly composed of N 2*p* states with a slight contribution from C_C 2*p* states, while the CBM in the spin-up channel consists equally of C_N 2*p* and N 2*p* states. Additionally, the PDOS displays a completely spin-polarized condition with a magnetic moment of 4.00 μ_B. As a ferromagnetically stable Pca21 C_4N_3 monolayer [32], its magnetic performance mainly originates from the 2*p* states of C_C and nitrogen electrons, where all nitrogen electrons contribute more to the total magnetic moment than C_C electrons (Figure 1a). The distribution of PDOS near the band edge for the Pca21 C_4N_3 monolayer may be due to the atomic ratio of C_C, C_N, and N in its unit cell being 1:3:3, along with the presence of unpaired electrons and lone pair electrons on nitrogen atoms. The spatial spin density distribution provides detailed information on the magnetic moment distribution of the system in real space. As shown in Figure 1b, the spatial spin density of the Pca21 C_4N_3 monolayer reveals that the magnetic moments are mainly distributed on the 2*p* orbitals of nitrogen atoms and the $2p_z$ orbitals of C_C atoms, with almost no distribution on the C_N atoms. The magnetic moment distribution in this monolayer may, in turn, result from the different chemical environments around C_C and C_N, as well as the influence of lone pair electrons on nitrogen.

Although the valence band electrons far from E_f and high-energy conduction band (CB) states have been less studied in depth, these electronic states, together with those near the band edge, collectively provide information on the orbital hybridization of constituent atoms and the bonding characteristics between atoms in the material. To investigate the origin of magnetic performance, it is essential to understand the electronic structure in the low-energy region of the VB and the high-energy region of the CB of Pca21 C_4N_3. Given the presence of unpaired electrons in pristine Pca21 C_4N_3, the spin-resolved PDOSs for the 2*s* and 2*p* states of N, C_C, and C_N in the Pca21 C_4N_3 monolayer have been considered.

Based on the corrugated microscopic structure of Pca21 C_4N_3 discussed above, we can infer that the 2*s* and 2*p* orbitals of the nitrogen are approximately sp^3-hybridized, while the 2*s* and 2*p* orbitals of the carbon undergo sp^2 hybridization. Two N sp^3-hybridized orbitals overlap significantly with the sp^2-hybridized orbitals of two adjacent C_N atoms, forming strong σ bonds and corresponding σ^* anti-bonding states. Another sp^3-hybridized orbital of nitrogen is occupied by a lone pair of electrons, leaving one hybridized orbital singly

occupied by one electron. The lone pair electron cloud, being unbound by bonding orbitals, exhibits higher energy and expanded volume. Consequently, the energy level of nitrogen unpaired electron is elevated due to repulsion from the lone pair of electrons. In the local C_C-3C_N structure, the three sp^2 orbitals of C_C overlap, respectively, with one sp^2 orbital from the three C_N atoms, forming three σ bonds and three σ* anti-bonding states, leaving a C_C 2p_z orbital occupied by a single electron. For the C_N atom, after it forms three σ bonds and σ* anti-bonding states with a neighboring carbon and two nitrogen atoms through their respective overlapping hybrid orbitals, the C_N also retains one unpaired electron. Due to the higher electronegativity of nitrogen (Pauling scale 3.04) compared to carbon (2.55), the bonding electron cloud in the C_N-N bond shifts towards the N. Consequently, besides the partial C_N-N σ bonding electronic states shifting to a lower energy region (corresponding to the σ_1 energy region in Figure 2a,c), the singly occupied 2p_z orbital level of C_N is lowered relative to that of C_C. Therefore, the singly occupied orbital energy levels of C_N and N are closer to each other than those of C_N and C_C. Most of the singly occupied states of C_N overlap with those of the two N atoms, while the remaining overlap with those of C_C, forming π bonds and π* anti-bonding states; thus, all singly occupied orbitals of C_N bond with surrounding atoms. Although the remaining singly occupied states of C_C and N are close in energy, they hardly overlap due to their distance and poor orbital matching, resulting in singly occupied states located near the spin-up VBM, which are the source of magnetic performance. The σ bonding and σ* anti-bonding states are significantly split, corresponding to the lower energy region of the VB and the higher energy region of the CB, respectively (see Figure 2a–c). In contrast, the π and π* orbital energy levels are less split, corresponding to the higher energy region of the VB and the lower energy region of the CB (see Figure 2a–c). To clearly distinguish the bonding and anti-bonding states between the C_N-N bond and the C_C-C_N bond, we divided the 2*s* and 2*p* PDOSs of the C_C, C_N, and N in Pca21 C_4N_3 into different energy regions. As shown in Figure 2a–c, from low- to high-energy regions in the VB, there are σ bonding, π bonding, and non-bonding regions, while in the spin-up CB, from low- to high-energy regions, there are π* anti-bonding and σ* anti-bonding regions. The non-bonding region of the VB is mainly composed of the lone pair electrons on N and the single electron states on C_C and N, which determine the VBM. The π bonding energy region is divided into two segments, i.e., the π_1 low-energy region and the π_2 high-energy region. The π bonding electrons of the C_C-C_N primarily contribute to the π_2 energy region, while those of the C_N-N are distributed in both the π_1 and π_2 energy regions, with N 2*p* electrons contributing more to π_1 energy regions. In the σ bonding energy region, the σ bonding electrons of the C_C-C_N mainly reside in the σ_2 energy region, whereas those of the C_N-N are spread across both the σ_1 and σ_2 energy regions. The CB is divided into the π_1^*, π_2^*, and σ* energy regions. The π_1^* energy region mainly comprises the 2*p* states of N and C_N, while π_2^* primarily consists of the 2*p* states of C_C and C_N with a minor contribution from N 2*p*. The σ* energy region is located in the high-energy part of the CB. The spin-up CBM is determined by the π* state of C_N-N, whereas the spin-down CBM is governed by the non-bonding 2*p* states of C_C and N. From Figure 2a,b, it is evident that the contribution of the 2*p* electrons of a single C_C to the magnetic moment is greater than that of a single N. Furthermore, the presence of N 2*s* states in the VB non-bonding, π bond, and σ bond regions and the appearance of 2*s* states of C_C and C_N in the VB low-energy (σ) region confirm the hypothesis of orbital hybridization for C and N. According to the role in orbital hybridization and bonding, we find the 2*s* orbital does not contribute to the magnetic moment; therefore, we will only analyze the 2*p* states of each system in subsequent discussions to simplify the analysis.

Bader charge analysis quantitatively illustrates the net electron transfer number between bonding atoms due to differences in electronegativity. In Pca21 C_4N_3, one C_N has a net loss of 1.06 *e*, while the nitrogen atom has a net gain of 1.06 *e*. This indicates that the C_N-N bond has both ionic and covalent components. The net electron transfer for C_C is zero, indicating that the bonds formed between C_C and C_N are covalent bonds. The electron localization function (ELF) plot provides a more intuitive view of the bonding

situation in the Pca21 C_4N_3 monolayer due to electron redistribution. Figure 2d clearly illustrates that the bonding electrons around C_C are concentrated along the C_C-C_N bonds, showcasing D_3 symmetry. Additionally, the bonding electrons are focused along the C_N-N bond, with the lone pair electrons located at the apex of the $\angle C_N N C_N$ angle. Notably, the lone pair electrons of the three N in the six-membered microcycles are not coplanar, which implies that the singly occupied orbitals of the three nitrogen atoms are also asymmetrical. This may be due to the repulsion between the lone pair electrons on different nitrogen atoms, causing nitrogen atoms to stay as far apart as possible. Moreover, these lone pair electrons also influence the C_N-N bond electron distribution (see Figure 2d), agreeing well with the highly corrugated structure and implying that the 2*p* orbitals provided by nitrogen atoms at different positions for bonding are not the same.

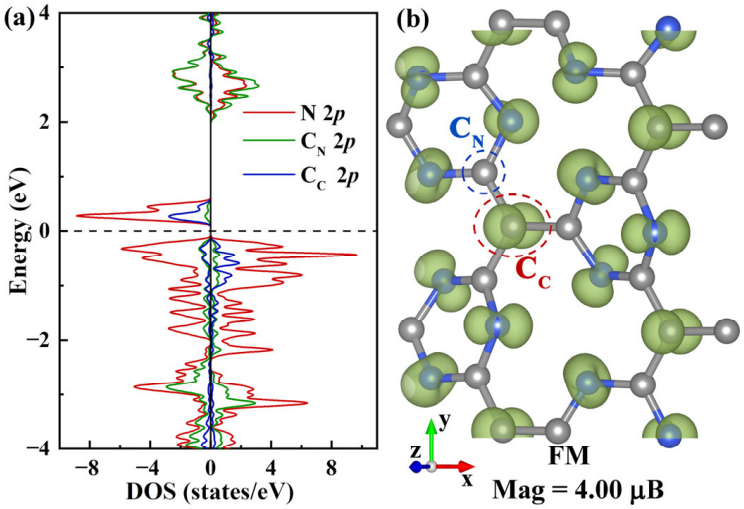


Figure 1. (**a**) The spin-polarized PDOS of C_C, C_N, and N 2*p* in the Pca21 C_4N_3 monolayer. The C_C 2*p*, C_N 2*p*, and N 2*p* states are represented by blue, green, and red lines, respectively. The Fermi level (E_f) is indicated by a black dashed line and set to 0 eV. This representation of E_f is also applicable to the subsequent density of states (DOS) plots. (**b**) The three-dimensional isosurfaces (iso-value of 0.01 e/Å^3) depicting net magnetization density (difference between spin-up and spin-down), which also applies to the subsequent net magnetization density, for the Pca21 C_4N_3 monolayer in the ferromagnetic state. Gray spheres symbolize C atoms, and blue spheres denote N atoms, which also applies to the subsequent Figures 2, 5 and 7. The subfigure labels represent the coordinates.

Based on the analysis described above, we recognize that the lone pair electrons on nitrogen atoms possess high energy and significant spatial extension. This characteristic not only impacts the energy levels of the singly occupied orbitals of N but also alters the composition of the singly occupied orbitals of N. To further investigate the origin and mechanism of magnetism, we analyzed the PDOSs of the $2p_x$, $2p_y$ and $2p_z$ orbitals for three N atoms (designated as N_{17}, N_{18}, and N_{19}, see Figure S1) of the six-membered microcycles in the Pca21 C_4N_3 monolayer, as well as those of the C_C and C_N atoms. The composition of the singly occupied orbitals and lone pair orbitals of the three N atoms (N_{17}, N_{18}, and N_{19}), varies significantly (see Figure 3a–c). The lone pair and unpaired electron orbitals of N_{17} are primarily composed of $2p_x$, $2p_y$, and $2p_z$ orbitals, with a larger proportion of the $2p_y$ orbital. For N_{18}, these electron orbitals are also formed by $2p_x$, $2p_y$, and $2p_z$ orbitals, but with a higher proportion of the $2p_y$ and $2p_z$ orbitals. In contrast, the N_{19} lone pair and unpaired electron orbitals mainly derive from the $2p_x$ and the $2p_z$ orbitals. The singly occupied states of the N atom located near the VBM serve as a part of the source of magnetic moment. As shown in Figure 3d, the $2p_z$ orbitals of C_N engage entirely in forming π and π^* anti-bonding states, with the π^* state contributing to the spin-up CBM. Figure 3e displays that the $2p_z$ orbital of C_C partially forms bonds, with the non-bonding occupied C_C $2p_z$ state located near the VBM as an additional source of magnetism, and the non-bonding

unoccupied C_C $2p_z$ corresponds to the spin-down CBM. Additionally, the C_C σ bonding states are composed of $2p_x$ and $2p_y$ orbitals, indicating that these orbitals participate in sp^2 hybridization.

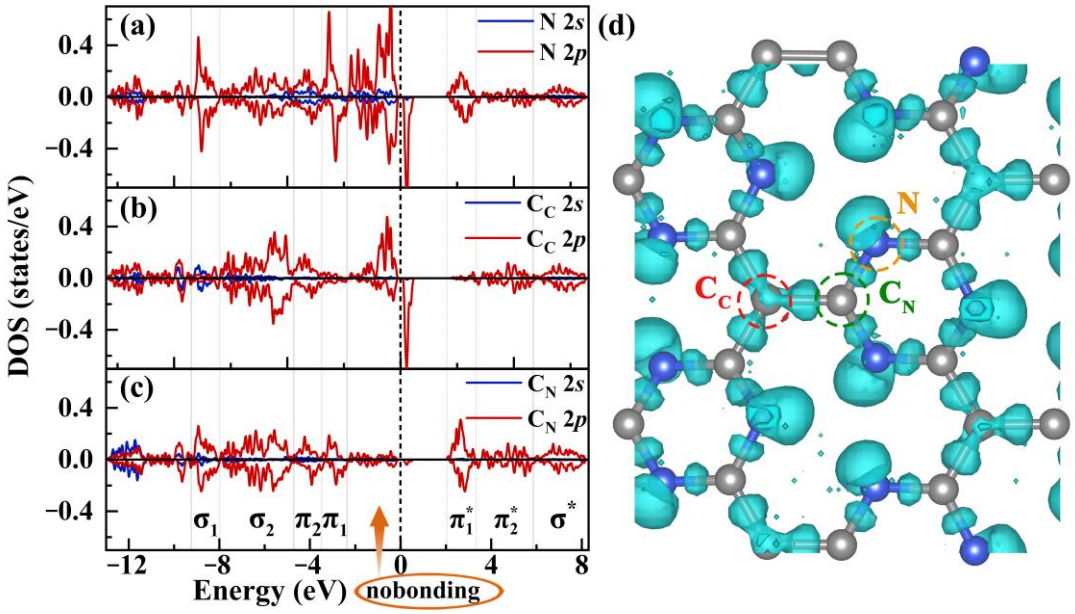


Figure 2. The spin-resolved PDOS diagrams for the 2*s* and 2*p* states of one (**a**) N, (**b**) C_C, and (**c**) C_N atom in the Pca21 C_4N_3 monolayer. The 2*s* and 2*p* states are represented by blue and red lines, respectively. (**d**) The ELF of Pca21 C_4N_3 monolayer, with cyan regions indicating electron accumulation. The isosurface value is set to 0.60 e/Å^3.

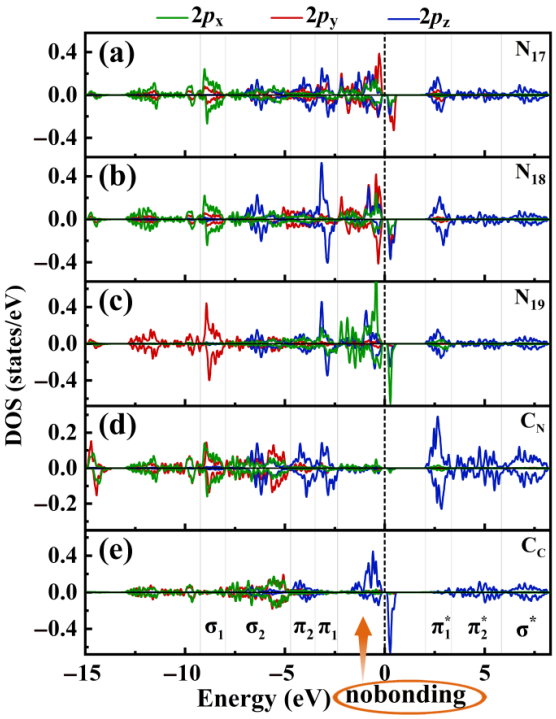


Figure 3. The spin-resolved PDOS of the $2p_x$, $2p_y$, and $2p_z$ for N (designated as (**a**) N_{17}, (**b**) N_{18}, and (**c**) N_{19}; see Figure S1), and (**d**) C_N, and (**e**) C_C in the Pca21 C_4N_3 monolayer. For C_C, C_N, and N, $2p_x$, $2p_y$ and $2p_z$ are represented by green, red, and blue lines, respectively.

2.2. The Electronic and Magnetic Modulation of Pca21 C_4N_3 Monolayer by Gas Adsorption

2.2.1. Stability and Magnetic Property of Pca21 C_4N_3 Monolayer with Nitric Oxide (NO) or Oxygen (O_2) Adsorption

To broaden the Pca21 C_4N_3 monolayer's application range, gas adsorption is used to modulate its magnetic properties. Gas adsorption can be classified into physisorption and chemisorption. Physisorption is achieved through van der Waals forces, while chemisorption relies on the formation of chemical bonds. Based on the structural characteristics of the Pca21 C_4N_3 monolayer (see Figure S1), five possible adsorption sites were considered: **N** (positioned above the N atom), $\mathbf{C_N}$ (positioned above the C_N atom), $\mathbf{C_C}$ (positioned above the C_C atom), **R1** (located above the center of the six-membered microcycle), and **R2** (located above the center of the twelve-membered microcycle). The gas molecules (NO or O_2) are initially oriented perpendicular to the monolayer surface. According to Equation 1, the adsorption energy (E_{ads}) for each adsorption configuration was calculated.

For the NO adsorption system (NO@C_4N_3), the comparison of the E_{ads} values shown in Figure 4a reveals the most stable adsorption configuration ($\mathbf{C_N}$ adsorption site), with the smallest E_{ads} value of −1.14 eV. The configuration of the NO@C_4N_3 system after being fully optimized is shown in Figure 5a. For convenience, NO is labeled as $(NO)_i$ before adsorption and as $(NO)_f$ after adsorption. Similarly, this notation applies to O_2, with $(O_2)_i$ before adsorption and $(O_2)_f$ after adsorption. In Figure 5a, the nitrogen atom of $(NO)_f$ (N_{ad}) is bonded with the nitrogen atom from the substrate (N_{sub}), and the value of $\angle N_{sub}N_{ad}O$ is 114.7°. The length of the N_{sub}-N_{ad} bond is 1.45 Å, and the N-O bond length increases from 1.17 Å before adsorption to 1.21 Å after adsorption. The net magnetic moment of the NO@C_4N_3 system is 2.99 μ_B at each adsorption site, which is less than the magnetic moment of pristine Pca21 C_4N_3 (4.00 μ_B). According to the Van Hove equation (Equation (2)), the desorption temperature for NO is determined to be 521.8 K, which is much higher than the T_C (247 K) of the Pca21 C_4N_3 monolayer [32]. This implies that within T_C, the adsorption of NO may lead to a reduction in the magnetic signal of Pca21 C_4N_3. Thus, the phenomenon of the weakening of magnetism within Tc could be judged as a necessary condition for NO adsorption on Pca21 C_4N_3. Therefore, Pca21 C_4N_3 has the potential to be developed as a NO gas sensor.

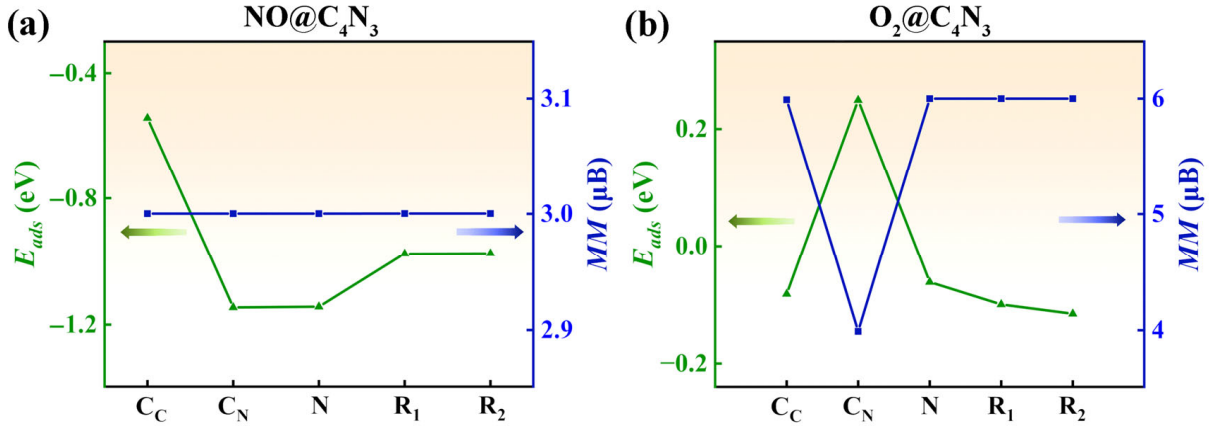


Figure 4. The adsorption energy and net magnetic moment of (**a**) NO@C_4N_3 systems and (**b**) O_2@C_4N_3 systems at different adsorption sites. The green lines denote adsorption energy, and the blue lines indicate the values of the magnetic moment.

For the O_2 adsorption system (O_2@C_4N_3), according to the adsorption energy values, the stability order of the five adsorption sites is $\mathbf{C_N}$ < **N** < $\mathbf{C_C}$ < **R1** < **R2**. As shown in Figure 4b, the E_{ads} of the $\mathbf{C_N}$ adsorption site is positive, indicating that this configuration does not exist. The E_{ads} values for the remaining four adsorption sites are negative, ranging from −0.06 to −0.11 eV. Among them, the **R2** adsorption site is the most stable, with an E_{ads} value of −0.11 eV. After optimization, the $(O_2)_f$ molecule is almost laid flat above the substrate. Based on the adsorption energy and the distance (2.79 Å) between the $(O_2)_f$

molecules and the Pca21 C_4N_3, it can be determined that they are physically adsorbed. Interestingly, the net magnetic moment of the O_2@C_4N_3 system at each adsorption site increases to 6.00 μ_B, increasing to 50% of the original sample.

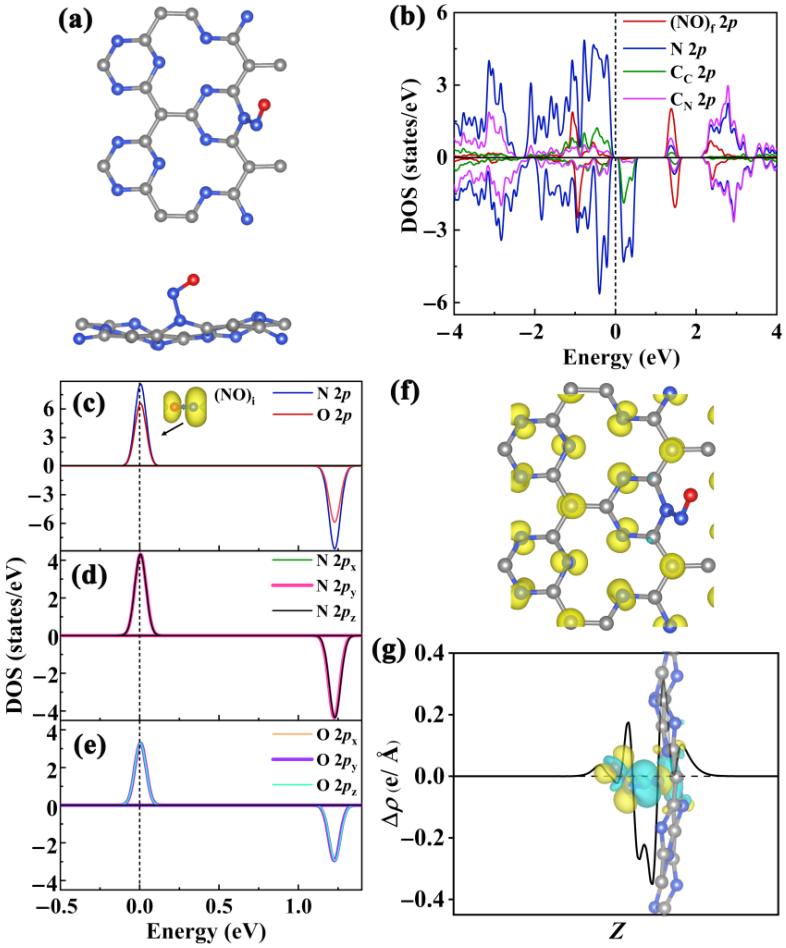


Figure 5. (**a**) The top (upper) and profile (lower) perspectives of the optimized configuration of the NO@C_4N_3 system. (**b**) The spin-resolved PDOS of 2*p* for $(NO)_f$, C_C, C_N, and N in the NO@C_4N_3 system. The 2*p* of $(NO)_f$ is denoted by red lines, and the C_C 2*p*, C_N 2*p*, and N 2*p* are denoted by blue, green, and pink lines, respectively. (**c**) In $(NO)_i$, the spin-resolved PDOS of N 2*p* and O 2*p* is represented by blue and red lines, respectively. The inset displays the spatial distribution of spin-up π^* orbitals for $(NO)_i$. In $(NO)_i$, (**d**) the PDOS of N $2p_x$, $2p_y$, and $2p_z$ is represented by green, rose, and black lines, respectively, and (**e**) the PDOS of O $2p_x$, $2p_y$, and $2p_z$ is represented by orange, purple, and cyan lines, respectively. (**f**) The views of the 3D isosurfaces (iso-value of 0.01 e/Å^3) of net magnetization density for the NO@C_4N_3. (**g**) Integrals of CDD along the *z* direction for the NO@C_4N_3 system. The inset depicts the CDD distributions, with yellow regions representing electron accumulation and cyan regions indicating electron depletion. The isosurface value is established at 5.00×10^{-3} e/Å^3. Red spheres denote O atoms, which also applies to the subsequent Figure 7.

Some previous studies [37–39] have highlighted the potential for stacking-induced functionality in similar crystalline materials, suggesting that interlayer interactions could provide further tunability. In order to investigate how stacking Pca21 C_4N_3 layers affects adsorption dynamics and magnetic responses in a system of NO or O_2 adsorbed on C_4N_3 bilayers, we considered two patterns for the NO or O_2 molecule adsorption, namely, interface and surface adsorption. For the interface adsorption, the gas molecule should cross the C_4N_3 monolayer to arrive at the interface region. As plotted in Figure S2a,b, it separately requires up to 6.04 eV and 3.72 eV for NO and O_2 gas molecules to penetrate the interlayer through the macrocycle of the Pca21 C_4N_3 monolayer, indicating this mode

of interface adsorption can be ruled out. As for the case of surface adsorption, based on our previous work [32], we established bilayer systems with three stacking configurations (AA, AB, and AC) to adsorb NO and O_2 gas molecules, respectively (see Figure S3), and calculated the corresponding adsorption energies [37–39] and magnetic moments, which are listed in Table S1. On the Pca21 C_4N_3 bilayer with AA, AB, and AC stacking configurations, the adsorption energies of the NO gas molecule are −1.26, −0.85, and −1.07 eV, respectively, while those of the O_2 gas molecule are 0.66, −0.11, and −0.44 eV, respectively. This indicates that interlayer interactions could provide tunability for the surface gas adsorption strength. However, interlayer interactions have a very weak effect on the net magnetic moments of these adsorption systems. The net magnetic moments of the systems with a NO gas molecule adsorbed on the C_4N_3 bilayer with the three stacking configurations are all almost 7.00 μ_B; meanwhile, the ones with O_2 gas molecule adsorption systems are all 10.00 μ_B. The bilayer systems with adsorbed NO and O_2 gas molecules have retained the ferromagnetic coupling characteristics of the pure bilayer systems [32]. Moreover, for the most stable adsorption configurations on the Pca21 C_4N_3 bilayer (NO on AA stacking pattern and O_2 on AC stacking pattern), the adsorption energies are similar to those of the Pca21 C_4N_3 monolayer. The change in magnetic moment for these most stable adsorption configurations on the Pca21 C_4N_3 bilayer is also similar to that of the monolayer system when compared to the pure bilayer. For example, the O_2 adsorption makes the magnetic moments of both the bilayer and monolayer systems increase by 2.00 μ_B. Therefore, in the following study on the magnetic regulation mechanism, we do not discuss the bilayer situation separately.

2.2.2. Electronic Structure of NO@C_4N_3 System

As shown in Figure 5b, the spin-down E_g of the most stable NO@C_4N_3 slightly decreases from 0.36 eV to 0.22 eV, with the spin-down CBM still originating from the 2*p* states of C_C and N. Meanwhile, the spin-up E_g significantly decreases from 2.24 eV to 1.36 eV. This notable change in the spin-up bandgap is due to the CBM of the NO@C_4N_3 system being composed of the 2*p* states of $(NO)_f$ as well as the N 2*p* and C 2*p* states. The magnetic property of the NO@C_4N_3 system still primarily originates from the N 2*p* and C_C 2*p* state electrons. In order to study the magnetic moment distribution and the mechanism of magnetic changes in the NO@C_4N_3 system, the PDOS, spatial spin density distribution, charge difference density (CDD), and Bader charge of NO and the most stable NO@C_4N_3 system were systematically investigated. As shown in Figure 5c, the magnetic moment of $(NO)_i$ is 1.00 μ_B, primarily originating from the partially occupied 2*p* states of N and O below the Fermi level, with the contribution from the N 2*p* states being greater than that from the O 2*p* states. The N 2*p* states are composed of $2p_y$ and $2p_z$ (Figure 5d), while the O 2*p* states also consist of $2p_y$ and $2p_z$ (Figure 5e). Figure 5f illustrates the magnetic moment distribution of the NO@C_4N_3 system. The spatial spin density for $(NO)_f$ and N_{sub} vanishes, contributing zero to the magnetic moment. The spatial spin density around the C_C atoms near N_{sub} ($C_{C\text{-}near}$) decreases, indicating a reduced contribution to the magnetic moment from these $C_{C\text{-}near}$ atoms. Meanwhile, the spin density distribution in the regions far from N_{sub} remains virtually unaffected, continuing to be dispersed on the C_C and N atoms. The CDD plot illustrates the changes in charge distribution induced by the formation of the new N_{sub}-N_{ad} chemical bond. As depicted in Figure 5g, certain regions experience an increase in electron density (yellow areas), while other regions show a decrease (cyan areas). Notably, the electron density decreases in the bonding region of N_{sub}-N_{ad}, whereas the non-bonding regions of N_{sub}, N_{ad}, and O exhibit an increase in electron density. The decrease in electron density in the N_{sub}-N_{ad} bonding region may be attributed to the fact that, before bonding with N_{ad}, this region was primarily occupied by the lone pair electrons, π electrons, and single electrons of N_{sub}. After bonding, the orbitals of the lone pair electrons change. Although this region is now a bonding area occupied by two bonding electrons, the number of electrons in this region is reduced compared to its original state, thus appearing as an electron-depleted area. The increase in electron density in some non-bonding regions of

N_{sub}, N_{ad}, and O may be attributed to these areas becoming occupied by lone pair electrons. Near the N_{sub} of the substrate, electron accumulation (yellow areas) and depletion (cyan areas) indicate that NO adsorption causes electron transfer, redistributing electron density and forming stable chemisorption. Although the N_{sub}-N_{ad} bond is formed by the same element, Bader charge analysis still shows a transfer of 0.058 e from the substrate to $(NO)_f$. This can be attributed to the differences in electronegativity, namely, O (Pauling scale: 3.44) > N > C. The bonding electron cloud of the C-N_{sub} bond shifts towards N_{sub}, while that of the N_{ad}-O bond shifts towards O. As a result, the electronegativity of N_{ad} is slightly higher than that of N_{sub}. When forming the N_{sub}-N_{ad} bond, the overall effect is the net electron transfer from N_{sub} to N_{ad}. The reason for the reduction in the magnetic moment of the NO@C_4N_3 system seems to differ from that of TCNQ-doped CrI_3. For TCNQ-CrI_3, the doping holes fill the half-occupied t_{2g} orbitals [40]. However, the mechanisms are similar: adsorption or doping leads to single-electron pairing, resulting in a reduced magnetic moment.

To further investigate the mechanism behind the magnetic changes in the NO@C_4N_3 system, we calculated the PDOS of 2*p* orbitals for NO before and after adsorption, as well as the PDOS of 2*p* orbitals for N_{sub}, $C_{C\text{-}near}$, and $C_{N\text{-}near}$ (the C_N adjacent to N_{sub}) within the NO@C_4N_3 system (see Figure 6). In $(NO)_i$, the $2p_x$ orbitals of N and O have a significant head-to-head overlap along the bond axis, forming a strong σ bond occupied by electrons. Meanwhile, the $2p_y$ and $2p_z$ orbitals of N and O overlap side-by-side, forming two π bonding orbitals occupied by electrons and two partially occupied π^* anti-bonding orbitals. The π bonding orbitals have a greater contribution from the O 2*p* states, while the π^* anti-bonding orbitals have a greater contribution from the N 2*p* states (see Figures 5c and 6a). The energy levels of the two spin-up π^* orbitals are degenerate and lower than those of the two spin-down degenerate π^* orbitals. The two spin-up π^* orbitals are occupied by only one electron, resulting in a magnetic moment of 1.00 μ_B. The bonding and anti-bonding states of the $(NO)_i$ molecule exhibit strong localization, and the Fermi level divides the spin-up π^* states (see Figures 5c and 6a). After adsorption, due to the formation of the N_{sub}-N_{ad} bond, the orbitals of N_{ad} can be approximated as sp^3-hybridized. The interaction between N_{ad} and O can be understood as consisting of one σ bond and one π bond, along with an orbital containing a lone pair of electrons and another orbital occupied by a single electron. The overlap of these two singly occupied orbitals forms a π bond occupied by two electrons and an empty π^* state. Therefore, after adsorption, the magnetic properties of $(NO)_f$ disappear. In $(NO)_f$, the lone pair electrons on N_{ad} and O are located at the $\angle N_{sub}N_{ad}O$ angle and on O (as shown in Figure 5g). Compared to the PDOS of $(NO)_i$ (Figure 6a), due to changes in bonding properties and the influence of the substrate, the 2*p* states of N_{ad} and O become more delocalized (see Figure 6b). Figure 6c shows the distribution of the $N_{sub}2p$ states and provides information about its bonding. After adsorption, in addition to containing a lone pair of electrons, N_{sub} forms three σ bonds with surrounding atoms, the N_{sub}-N_{ad} bond and two N_{sub}-$C_{N\text{-}near}$ bonds, thereby achieving an eight-electron stable state. Consequently, N_{sub} contributes zero magnetic moment to the NO@C_4N_3 system. Constrained by these three strong σ bond orbitals, the corresponding σ bonding electrons shift to lower energy levels. Due to the absence of its own non-bonding single electron, the lone pair electrons on N_{sub} experience a reduction in energy. The position and shape of this lone pair orbital are altered due to the influence of the formed N_{sub}-N_{ad} bond (see Figure 5g). After adsorption, the atoms providing paired electrons for the singly occupied orbital of $C_{N\text{-}near}$ decrease from three (two N and one C_C) to two ($C_{C\text{-}near}$ and N). Consequently, the proportion of paired electrons from these two atoms increases, reducing the contribution of $C_{C\text{-}near}$ to the system's magnetism (see Figure 6e). Under the influence of NO chemisorption, $C_{N\text{-}near}$ 2*p* states (see Figure 6d), N_{sub} 2*p* states (see Figure 6c), and C_C 2*p* states (see Figure 6e) are induced below the original system's CBM. These induced 2*p* states, along with the 2*p* states of $(NO)_f$, form the spin-up CBM of the NO@C_4N_3 system, significantly reducing the spin-up bandgap. In summary, the N_{sub}-N_{ad} chemical bond is formed between the $(NO)_f$ and the substrate, leading to significant changes in the bonding nature and electron distribution of N_{sub}, N_{ad}, and O.

As a result, $(NO)_f$ and N_{sub} no longer have orbitals occupied by unpaired electrons and thus do not contribute to the magnetic moment. Additionally, the contributions of $C_{C\text{-}near}$ to the magnetic moment are also reduced. Furthermore, the CBM of the adsorption system is mainly composed of the 2*p* state of $(NO)_f$ and its induced electronic states, resulting in a significant reduction in the spin-up bandgap. This reduced bandgap helps to enhance the photoresponse to some extent.

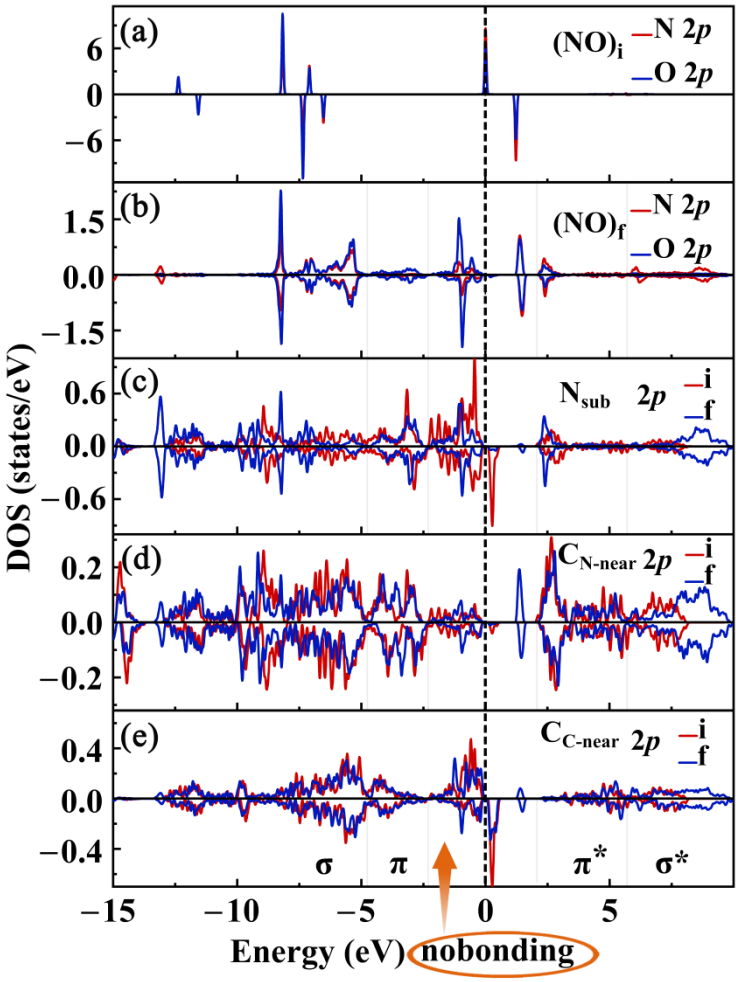


Figure 6. The spin-resolved PDOS of N 2*p* (denoted with red lines) and O 2*p* (denoted with blue lines) in (**a**) $(NO)_i$ and (**b**) $(NO)_f$; $(NO)_i$ and $(NO)_f$ denote NO before and after adsorption on Pca21 C_4N_3, respectively. The spin-resolved PDOS of 2*p* for N_{sub} (**c**), $C_{C\text{-}near}$ (**d**), and $C_{N\text{-}near}$ (**e**) in systems; the red lines labeled with **i** denote the 2*p* sates before NO adsorption, and the blue lines labeled with **f** represent the 2*p* after NO adsorption. N_{sub} refers to the N in the C_4N_3 substrate bonded with the NO molecule, $C_{C\text{-}near}$ is C_C adjacent to N_{sub}, and $C_{N\text{-}near}$ is C_N neighboring N_{sub}.

2.2.3. Electronic Structure of O_2@C_4N_3 System Through Magnetic Coupling Between O_2 and C_4N_3 Pca21 C_4N_3 Monolayer

To investigate the impact of O_2 adsorption on the electronic structure and magnetic distribution of the Pca21 C_4N_3 monolayer, we studied the DOS, CDD, and spin density distribution of the most stable O_2@C_4N_3 system. Compared to the pristine Pca21 C_4N_3, the spin-up E_g of the O_2-adsorbed system slightly decreases from 2.24 eV to 2.22 eV, while the spin-down E_g slightly increases from 0.36 eV to 0.42 eV. As shown in Figure 7a, the contribution of the O orbitals in both spin channels is primarily concentrated in the deep-level regions (below −1.00 eV and above 1.00 eV). Near the Fermi level, the DOS peak for $(O_2)_f$ is sharp and narrow, exhibiting strong localization, which indicates that it is minimally affected by the substrate. This also indirectly suggests that the interaction between the O_2

gas and the substrate is mainly due to physical adsorption. The CDD map (see Figure 7b) shows that weak interactions between O_2 molecules and the substrate cause slight changes in the spatial electron distribution. There are small regions of electron accumulation (yellow areas) and depletion (cyan areas) on both the substrate and $(O_2)_f$. Compared with the magnetic moment distribution of the pristine Pca21 C_4N_3 monolayer (see Figure 1b) and $(O_2)_i$ (see the inset of Figure 7d), the magnetic moment distribution of the substrate and $(O_2)_f$ (Figure 7c) is almost unaffected, with the magnetic moments still located on the $(O_2)_f$ molecules and the substrate's magnetic moments still distributed on N and C_C.

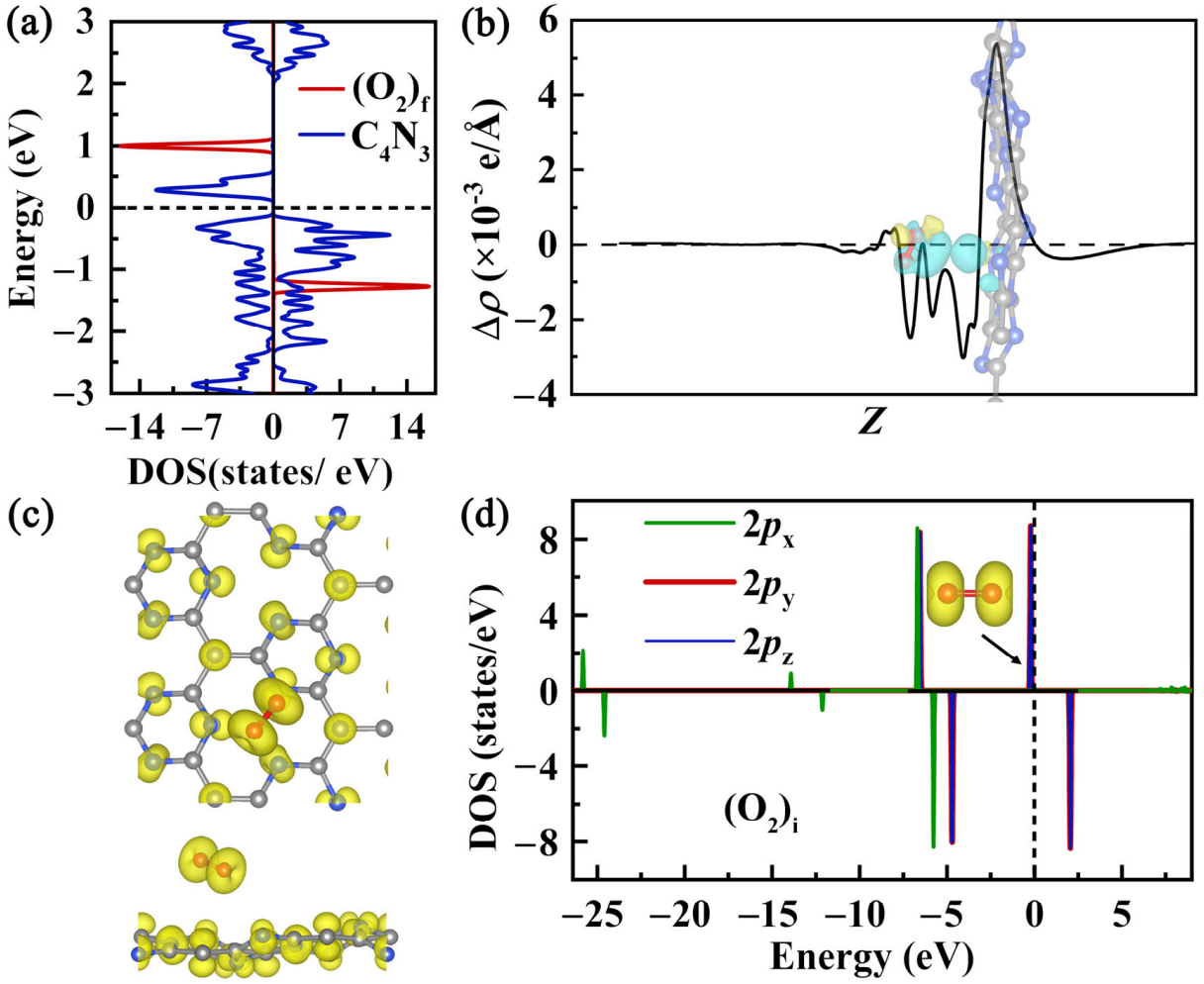


Figure 7. (**a**) The PDOSs for $(O_2)_f$ and C_4N_3 in the $O_2@C_4N_3$ system, which are represented by blue and red lines, respectively. (**b**) Integrals of CDD along the z direction for the $O_2@C_4N_3$ system. The inset depicts the CDD distributions, with yellow regions representing electron accumulation and cyan regions indicating electron depletion. The isosurface value is established at 2.00×10^{-3} e/Å^3. (**c**) The top (upper) and profile (lower) views of the 3D isosurfaces (the iso-value is 1.15×10^{-2} e/Å^3) of net magnetization density for the $O_2@C_4N_3$ monolayer. (**d**) The spin-resolved PDOSs of the $2p_x$, $2p_y$, and $2p_z$ for $(O_2)_i$, which are represented by green, red, and blue lines, respectively. The inset displays the spatial distribution of spin-up π^* orbitals for $(O_2)_i$.

In order to investigate the interaction between O_2 and the substrate, we calculated the PDOS of the $2p_x$, $2p_y$, and $2p_z$ orbitals of $(O_2)_I$; the spin density distribution of O_2; and the PDOS of the $2p$ orbitals of the three N, three C, and six C_N atoms in the twelve-membered microcycle below the **R2** adsorption site. According to the PDOS of $(O_2)_i$ (Figure 7d), it can be inferred that the $2p_x$ orbitals of the two O atoms overlap head-to-head, resulting in a large energy splitting into σ bonding and σ^* anti-bonding orbitals. The $2p_y$ and $2p_z$ orbitals of the two O atoms overlap side-by-side, forming two π bonding orbitals and two π^*

anti-bonding orbitals with smaller energy splitting. The energy levels of the two spin-up π^* orbitals are degenerate and lower than those of the two spin-down degenerate π^* orbitals. The two spin-up π^* orbitals are occupied by two electrons, leaving the two spin-down π^* anti-bonding orbitals empty, resulting in a magnetic moment of 2.00 μ_B. The 2.00 μ_B magnetic moment of $(O_2)_i$ is uniformly distributed in the spin-up π^* anti-bonding orbitals (see the inset in Figure 7d). The highest occupied molecular orbital (HOMO) energy level of $(O_2)_i$ is −6.78 eV. After adsorption, due to the magnetic attraction from the substrate, the HOMO energy level of $(O_2)_f$ shifts down by 0.04 eV. Compared to the initial state, the 2*p* PDOSs of $(O_2)_f$ for spin-up and spin-down π^* anti-bonding orbitals show increased peaks near the Fermi level, but the broadening remains narrow (see Figure S4a), indicating strong localization of oxygen electronic states. At the substrate adsorption site, the PDOSs of 2*p* for the C and N atoms in the twelve-membered microcycle show almost no noticeable change (see Figure S4b–d). Theoretically, the 2*p* PDOS of these C and N atoms should exhibit a slight shift towards lower energy levels. However, due to the extremely weak magnetic interaction of the $(O_2)_f$ molecule, any changes in the PDOS are difficult to discern. This further demonstrates that the interaction between $(O_2)_f$ and the substrate is physisorption.

From the above analysis, it is evident that in the pristine Pca21 C_4N_3 system, the combined contribution of three N atoms to the system's magnetic moment is greater than that of one C_C (Figure 1a). However, the contribution of an individual C_C exceeds that of a single N atom (Figure 2a,b). Consequently, the qualitative order of the net magnetic moment for the five adsorption sites on the substrate, from smallest to largest, can be determined as $\mathbf{C_N} < \mathbf{N} < \mathbf{C_C} < \mathbf{R1} < \mathbf{R2}$. This order perfectly aligns with the stability sequence of the five adsorption sites. This implies that the interaction between the $(O_2)_f$ molecule and the substrate is primarily driven by magnetic interactions, specifically characterized by the repulsion between like magnetic poles and the attraction between opposite magnetic poles. For the most stable O_2@Pca21 C_4N_3 system, the adsorption of O_2 significantly enhances the system's magnetic moment, increasing from 4.00 μ_B to 6.00 μ_B, indicating that a ferromagnetic coupling may exist between the $(O_2)_f$ and the substrate. In order to confirm this point, we calculate the energy difference between the ferromagnetic state and antiferromagnetic states. The results show that the total energy of the system in the ferromagnetic state (E_{FM}) is 0.08 eV lower than that in the antiferromagnetic state (E_{AFM}), i.e., $E_{FM} - E_{AFM} = -0.08$ eV. The ferromagnetic coupling may also explain why the **R2** site is the most stable adsorption site for the O_2 gas molecule. Specifically, when $(O_2)_i$ is positioned at the **R2** site, which has the largest magnetic moment among the five adsorption sites, the magnetic interaction is the strongest, resulting in the lowest adsorption energy and the most stable system.

3. Computation Details

The fundamental calculations were performed using density functional theory (DFT) with the Vienna ab initio Simulation Package (VASP) [41]. The exchange-correlation function was handled using the Perdew–Burke–Ernzerhof (PBE) form within the generalized gradient approximation (GGA) [42]. The projector augmented wave (PAW) method was used to model electron–ion interactions [43]. Van der Waals (vdW) corrections were included using the DFT-D3 method as described by Grimme [44,45]. A vacuum layer greater than 20 Å in the non-periodic direction prevented interactions between periodic images. Geometry optimizations involved relaxing every atom in the supercell, applying a force convergence criterion of 0.05 eV/Å and a total energy convergence of 10^{-5} eV. A $5 \times 5 \times 1$ Monkhorst-Pack k-point mesh was employed to sample the Brillouin zone. The plane-wave basis set cutoff for the electron wave functions was fixed at 500 eV.

The adsorption energy E_{ads} for a single gas molecule on the Pca21 C_4N_3 monolayer is defined as

$$E_{ads} = E_{total} - E_{gas} - E_{C_4N_3} \quad (1)$$

where E_{total}, E_{gas}, and $E_{C_4N_3}$ are the total energy of the adsorption system, isolated NO gas molecule, and pristine Pca21 C_4N_3 monolayer, respectively. Based on the definition of

adsorption energy, the lower the adsorption energy of the adsorption system, the higher its stability.

In order to evaluate the thermal stability and reversibility of the NO@C_4N_3 configuration in practical applications, the Van Hove equation was employed to estimate the desorption temperature T_d, as indicated below:

$$T_d = \left(\frac{|E_{ads}|}{k_B}\right)\left(\frac{\Delta S}{R} - \ln\frac{P}{P_0}\right)^{-1} \quad (2)$$

where R represents the universal gas constant, k_B stands for the Boltzmann constant, E_{ads} indicates the adsorption energy, P is the atmospheric pressure, $P = P_0 = 1$ atm, and ΔS denotes the entropy change associated with the phase transition of NO from liquid to gas and its value of 210.8 $J{\cdot}K^{-1}{\cdot}mol^{-1}$ is obtained from the handbook in [46].

4. Conclusions

First-principles calculations were conducted to systematically investigate the magnetic mechanism and magnetic regulation of a 2D organic semiconductor Pca21 C_4N_3 monolayer by adsorbing magnetic polar NO or non-polar O_2 gas molecules. The calculated result reveals that the magnetic moment of the Pca21 C_4N_3 monolayer with ferromagnetic stability originates from the C_C $2p_z$ and N $2p$ electrons due to the influence of the lone pair electrons on nitrogen atoms. For the most stable NO@Pca21 C_4N_3 system, the adsorption of NO pairs an unpaired electron from the substrate nitrogen atoms with a single magnetic electron in the NO molecule, forming a N_{sub}-N_{ad} chemical bond. This interaction significantly reduces the system's magnetic moment from 4.00 to 2.99 μ_B, decreases the spin-down E_g from 0.36 to 0.22 eV, and the spin-up E_g greatly decreases from 2.24 to 1.36 eV. The desorption temperature for NO is 521.8 K, much higher than the T_C (247 K) of the Pca21 C_4N_3 monolayer. Therefore, NO gas adsorption can effectively modulate the electronic and magnetic properties of the Pca21 C_4N_3 monolayer, suggesting its potential application as a gas sensor by monitoring changes in magnetic and electronic properties. For the stable O_2@Pca21 C_4N_3 system, no chemical bond is formed between $(O_2)_f$ and the substrate, and their weak interaction from magnetic pole attraction has a negligible effect on the electronic structure of the system. However, O_2 exhibits ferromagnetic coupling with the substrate, enhancing the system's magnetic moment from 4.00 to 6.00 μ_B. Our comprehensive findings not only reveal the magnetic mechanism in the Pca21 C_4N_3 monolayer, but also uncover a simple and cost-effective method to regulate its magnetic moment, as well as its potential application as a NO gas sensor. These insights provide crucial theoretical foundations and research directions for emphasizing the significance of the Pca21 C_4N_3 monolayer in the realm of low-dimensional magnetic materials and expanding its application potential.

Supplementary Materials: The following supporting information can be downloaded at https://www.mdpi.com/article/10.3390/molecules29215194/s1: Figure S1: Top and side views of the Pca21 C_4N_3 monolayer; Figure S2: The energy barriers for NO and O_2 diffusion in the 12-membered macrocycles of Pca21 C_4N_3 monolayer; Figure S3: The top and side views of NO and O_2 adsorbed on AA, AB, and AC stacking patterns for the Pca21 C_4N_3 bilayer; Figure S4: The spin-resolved PDOS of $2p$ for O_2, and three N, three C_C and six C_N in the 12-membered microcycles at the R2 adsorption configuration; Table S1: The net magnetic moment and adsorption energy for NO and O_2 adsorbed on C_4N_3 monolayer and bilayer with different stacking patterns.

Author Contributions: Supervision, X.T. and L.J.; Formal analysis, D.Z. and L.J.; Investigation, D.Z. and H.Y.; Writing, D.Z., X.T. and L.J.; Review and editing, X.T. and S.L.; Calculation, X.G., W.X. and S.L.; Visualization, X.T.; Funding acquisition, D.Z., S.L. and L.J. All authors have read and agreed to the published version of the manuscript.

Funding: This study was funded by the Young Scientist Project of Henan Province (Grant No. 225200810103), the Program for Science & Technology Innovation Talents in Universities of Henan Province (Grant No. 24HASTIT013), the College Students Innovation Fund of Anyang Normal University (Grant No. 202410479044), the Henan College Key Research Project (Grant Nos. 24B430005 and 24A430002), the Natural Science Foundation of Henan Province (Grant No. 232300420128), the Scientific Research Innovation Team Project of Anyang Normal University (Grant No. 2023AYSYKY-CXTD04), the 2023 Teaching Research Project of the Physics Teaching Steering Committee for Higher Education Institutions, Exploration and Implementation of Ideological and Political Education in Thermodynamics Courses (Grant No. JZW-23-RX-16), and the Scientific and Technological Project of Anyang City (Grant No. 2023C01GX009).

Institutional Review Board Statement: Not applicable.

Informed Consent Statement: Not applicable.

Data Availability Statement: Data are contained within the article and Supplementary Materials.

Conflicts of Interest: The authors declare no conflicts of interest.

References

1. Wang, Z.; Tang, C.; Sachs, R.; Barlas, Y.; Shi, J. Proximity-Induced Ferromagnetism in Graphene Revealed by the Anomalous Hall Effect. *Phys. Rev. Lett.* **2015**, *114*, 016603. [CrossRef] [PubMed]
2. Gong, C.; Li, L.; Li, Z.; Ji, H.; Stern, A.; Xia, Y.; Cao, T.; Bao, W.; Wang, C.; Wang, Y.; et al. Discovery of intrinsic ferromagnetism in two-dimensional van der Waals crystals. *Nature* **2017**, *546*, 265–269. [CrossRef] [PubMed]
3. Huang, B.; Clark, G.; Navarro-Moratalla, E.; Klein, D.R.; Cheng, R.; Seyler, K.L.; Zhong, D.; Schmidgall, E.; McGuire, M.A.; Cobden, D.H.; et al. Layer-dependent ferromagnetism in a van der Waals crystal down to the monolayer limit. *Nature* **2017**, *546*, 270–273. [CrossRef] [PubMed]
4. Song, Q.; Occhialini, C.A.; Ergeçen, E.; Ilyas, B.; Amoroso, D.; Barone, P.; Kapeghian, J.; Watanabe, K.; Taniguchi, T.; Botana, A.S.; et al. Evidence for a single-layer van der Waals multiferroic. *Nature* **2022**, *602*, 601–605. [CrossRef] [PubMed]
5. Xu, S.; Jia, F.; Yu, X.; Hu, S.; Gao, H.; Ren, W. Intrinsic multiferroic MnOF monolayer with room-temperature ferromagnetism. *Mater. Today Phys.* **2022**, *27*, 100775. [CrossRef]
6. Wang, B.; Zhang, X.; Zhang, Y.; Yuan, S.; Guo, Y.; Dong, S.; Wang, J. Prediction of a two-dimensional high-TC f-electron ferromagnetic semiconductor. *Mater. Horiz.* **2020**, *7*, 1623–1630. [CrossRef]
7. Tang, C.; Ostrikov, K.; Sanvito, S.; Du, A. Prediction of room-temperature ferromagnetism and large perpendicular magnetic anisotropy in a planar hypercoordinate FeB3 monolayer. *Nanoscale Horiz.* **2021**, *6*, 43–48. [CrossRef]
8. Han, F.; Yang, G. Ferromagnetism above room temperature in Janus Fe2X (X. = S, Se) monolayers. *J. Mater. Chem. C* **2024**, *12*, 6663–6670. [CrossRef]
9. Liu, C.; Wang, Y.; Li, H.; Wu, Y.; Li, Y.; Li, J.; He, K.; Xu, Y.; Zhang, J.; Wang, Y. Robust axion insulator and Chern insulator phases in a two-dimensional antiferromagnetic topological insulator. *Nat. Mater.* **2020**, *19*, 522–527. [CrossRef]
10. Xu, X.; Ma, Y.; Zhang, T.; Lei, C.; Huang, B.; Dai, Y. Prediction of two-dimensional antiferromagnetic ferroelasticity in an AgF2 monolayer. *Nanoscale Horiz.* **2020**, *5*, 1386–1393. [CrossRef]
11. Gong, Y.; Guo, J.; Li, J.; Zhu, K.; Liao, M.; Liu, X.; Zhang, Q.; Gu, L.; Tang, L.; Feng, X.; et al. Experimental Realization of an Intrinsic Magnetic Topological Insulator*. *Chin. Phys. Lett.* **2019**, *36*, 076801. [CrossRef]
12. Mukherjee, T.; Kar, S.; Ray, S.J. Tunable electronic and magnetic properties of two-dimensional magnetic semiconductor VIBr2. *Comput. Mater. Sci.* **2022**, *209*, 111319. [CrossRef]
13. Zhang, L.; Cui, Z. First-Principles Study of Metal Impurities in Silicon Carbide: Structural, Magnetic, and Electronic Properties. *Front. Mater.* **2022**, *9*, 56675. [CrossRef]
14. Zhang, L.; Cui, Z. Theoretical Study on Electronic, Magnetic and Optical Properties of Non-Metal Atoms Adsorbed onto Germanium Carbide. *Nanomaterials* **2022**, *12*, 1712. [CrossRef] [PubMed]
15. Shen, C.; Wang, G.; Wang, T.; Zhao, X.; Yan, Y.; Song, X.; Liu, X.; Wang, Y.; Xia, C. Tuning the magnetic anisotropy of ferromagnetic MnS2 monolayers via electron occupation of Mn d orbitals. *Phys. Rev. B* **2021**, *104*, 224406. [CrossRef]
16. Alsubaie, M.; Tang, C.; Wijethunge, D.; Qi, D.; Du, A. First-Principles Study of the Enhanced Magnetic Anisotropy and Transition Temperature in a CrSe2 Monolayer via Hydrogenation. *ACS Appl. Electron. Mater.* **2022**, *4*, 3240–3245. [CrossRef]
17. Li, L.; Qin, R.; Li, H.; Yu, L.; Liu, Q.; Luo, G.; Gao, Z.; Lu, J. Functionalized Graphene for High-Performance Two-Dimensional Spintronics Devices. *ACS Nano* **2011**, *5*, 2601–2610. [CrossRef]
18. Katekomol, P.; Roeser, J.; Bojdys, M.; Weber, J.; Thomas, A. Covalent Triazine Frameworks Prepared from 1,3,5-Tricyanobenzene. *Chem. Mater.* **2013**, *25*, 1542–1548. [CrossRef]

19. Tuček, J.; Błoński, P.; Sofer, Z.; Šimek, P.; Petr, M.; Pumera, M.; Otyepka, M.; Zbořil, R. Sulfur Doping Induces Strong Ferromagnetic Ordering in Graphene: Effect of Concentration and Substitution Mechanism. *Adv. Mater.* **2016**, *28*, 5045–5053. [CrossRef]
20. González-Herrero, H.; Gómez-Rodríguez, J.M.; Mallet, P.; Moaied, M.; Palacios, J.J.; Salgado, C.; Ugeda, M.M.; Veuillen, J.-Y.; Yndurain, F.; Brihuega, I. Atomic-scale control of graphene magnetism by using hydrogen atoms. *Science* **2016**, *352*, 437–441. [CrossRef]
21. Zhou, J.; Wang, Q.; Sun, Q.; Chen, X.S.; Kawazoe, Y.; Jena, P. Ferromagnetism in Semihydrogenated Graphene Sheet. *Nano Lett.* **2009**, *9*, 3867–3870. [CrossRef] [PubMed]
22. Vozmediano, M.A.H.; López-Sancho, M.P.; Stauber, T.; Guinea, F. Local defects and ferromagnetism in graphene layers. *Phys. Rev. B* **2005**, *72*, 155121. [CrossRef]
23. Hu, J.; Wu, R. Giant Magnetic Anisotropy of Transition-Metal Dimers on Defected Graphene. *Nano Lett.* **2014**, *14*, 1853–1858. [CrossRef] [PubMed]
24. Withers, F.; Dubois, M.; Savchenko, A.K. Electron properties of fluorinated single-layer graphene transistors. *Phys. Rev. B* **2010**, *82*, 073403. [CrossRef]
25. Huang, P.; Huang, J.; Pantovich, S.A.; Carl, A.D.; Fenton, T.G.; Caputo, C.A.; Grimm, R.L.; Frenkel, A.I.; Li, G. Selective CO_2 Reduction Catalyzed by Single Cobalt Sites on Carbon Nitride under Visible-Light Irradiation. *J. Am. Chem. Soc.* **2018**, *140*, 16042–16047. [CrossRef]
26. Jiang, X.; Liu, Y.; Wang, T.; Xia, B.; Qian, J.; Ran, J.; Zhang, Z.; Gao, D. High-temperature ferromagnetism in non-metal carbonitride: From nitrogen vacant g-C3N4 to N-doped graphene. *J. Magn. Magn. Mater.* **2021**, *538*, 168223. [CrossRef]
27. Gao, D.; Liu, Y.; Liu, P.; Si, M.; Xue, D. Atomically Thin B doped g-C(3)N(4) Nanosheets: High-Temperature Ferromagnetism and calculated Half-Metallicity. *Sci. Rep.* **2016**, *6*, 35768. [CrossRef]
28. Majumder, C.; Kumar Mondal, T.; Bhattacharya, S.; Saha, S.K. Observation of room temperature metal free ferromagnetism in sulfur doped graphitic carbon nitride. *J. Magn. Magn. Mater.* **2022**, *559*, 169439. [CrossRef]
29. Du, L.; Gao, B.; Xu, S.; Xu, Q. Strong ferromagnetism of g-C_3N_4 achieved by atomic manipulation. *Nat. Commun.* **2023**, *14*, 2278. [CrossRef]
30. Wang, Y.; Guo, Y.; Wang, Z.; Fu, L.; Zhang, Y.; Xu, Y.; Yuan, S.; Pan, H.; Du, Y.; Wang, J.; et al. Realization of Strong Room-Temperature Ferromagnetism in Atomically Thin 2D Carbon Nitride Sheets by Thermal Annealing. *ACS Nano* **2021**, *15*, 12069–12076. [CrossRef]
31. He, C.; Liao, Y.; Ouyang, T.; Zhang, H.; Xiang, H.; Zhong, J. Flat-band based high-temperature ferromagnetic semiconducting state in the graphitic C4N3 monolayer. *Fundam. Res.* **2023**. [CrossRef]
32. Zhao, D.; Tang, X.; Xing, W.; Zhang, Y.; Gao, X.; Zhang, M.; Xie, Z.; Yan, X.; Ju, L. Designing Organic Spin-Gapless Semiconductors via Molecular Adsorption on C4N3 Monolayer. *Mol.* **2024**, *29*, 3138. [CrossRef] [PubMed]
33. Nair, R.R.; Tsai, I.L.; Sepioni, M.; Lehtinen, O.; Keinonen, J.; Krasheninnikov, A.V.; Castro Neto, A.H.; Katsnelson, M.I.; Geim, A.K.; Grigorieva, I.V. Dual origin of defect magnetism in graphene and its reversible switching by molecular doping. *Nat. Commun.* **2013**, *4*, 2010. [CrossRef] [PubMed]
34. Zhang, R.; Li, B.; Yang, J. A First-Principles Study on Electron Donor and Acceptor Molecules Adsorbed on Phosphorene. *J. Phys. Chem. C* **2015**, *119*, 2871–2878. [CrossRef]
35. Zhu, J.; Ha, E.; Zhao, G.; Zhou, Y.; Huang, D.; Yue, G.; Hu, L.; Sun, N.; Wang, Y.; Lee, L.Y.S.; et al. Recent advance in MXenes: A promising 2D material for catalysis, sensor and chemical adsorption. *Coord. Chem. Rev.* **2017**, *352*, 306–327. [CrossRef]
36. Cai, Y.; Zhou, H.; Zhang, G.; Zhang, Y.-W. Modulating Carrier Density and Transport Properties of MoS2 by Organic Molecular Doping and Defect Engineering. *Chem. Mater.* **2016**, *28*, 8611–8621. [CrossRef]
37. Constantinescu, G.; Kuc, A.; Heine, T. Stacking in Bulk and Bilayer Hexagonal Boron Nitride. *Phys. Rev. Lett.* **2013**, *111*, 036104. [CrossRef] [PubMed]
38. Kuc, A.; Springer, M.A.; Batra, K.; Juarez-Mosqueda, R.; Wöll, C.; Heine, T. Proximity Effect in Crystalline Framework Materials: Stacking-Induced Functionality in MOFs and COFs. *Adv. Funct. Mater.* **2020**, *30*, 1908004. [CrossRef]
39. Zhang, Y.; Položij, M.; Heine, T. Statistical Representation of Stacking Disorder in Layered Covalent Organic Frameworks. *Chem. Mater.* **2022**, *34*, 2376–2381. [CrossRef]
40. Tang, C.; Zhang, L.; Du, A. Tunable magnetic anisotropy in 2D magnets via molecular adsorption. *J. Mater. Chem. C* **2020**, *8*, 14948–14953. [CrossRef]
41. Kresse, G.; Furthmüller, J. Efficient iterative schemes for ab initio total-energy calculations using a plane-wave basis set. *Phys. Rev. B* **1996**, *54*, 11169–11186. [CrossRef] [PubMed]
42. Perdew, J.P.; Burke, K.; Ernzerhof, M. Generalized Gradient Approximation Made Simple. *Phys. Rev. Lett.* **1996**, *77*, 3865–3868. [CrossRef] [PubMed]
43. Blöchl, P.E. Projector augmented-wave method. *Phys. Rev. B* **1994**, *50*, 17953–17979. [CrossRef] [PubMed]
44. Grimme, S. Semiempirical GGA-type density functional constructed with a long-range dispersion correction. *J. Comput. Chem.* **2006**, *27*, 1787–1799. [CrossRef]

45. Liu, S.; Yin, H.; Liu, P.-F. Strain-dependent electronic and mechanical properties in one-dimensional topological insulator Nb_4SiTe_4. *Phys. Rev. B* **2023**, *108*, 045411. [CrossRef]
46. Lide, D.R. *Handbook of Chemistry and Physics*; CRC Press: New York, NY, USA, 2003.

Disclaimer/Publisher's Note: The statements, opinions and data contained in all publications are solely those of the individual author(s) and contributor(s) and not of MDPI and/or the editor(s). MDPI and/or the editor(s) disclaim responsibility for any injury to people or property resulting from any ideas, methods, instructions or products referred to in the content.